IEEE Photonics Journal
An IEEE Photonics Society Publication

Complete Mode Structure Analysis of Tilted Bragg Grating Refractometers in Planar Waveguides Toward Absolute Index Measurement

Volume 3, Number 5, October 2011

Keith R. Daly
Christopher Holmes
James C. Gates
Peter G. R. Smith
Giampaolo D'Alessandro

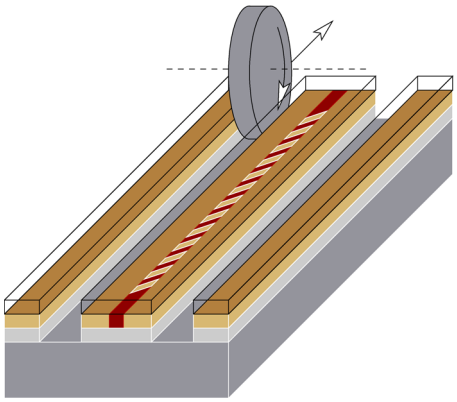

DOI: 10.1109/JPHOT.2011.2168515
1943-0655/$26.00 ©2011 IEEE

IEEE photonics SOCIETY

IEEE

Complete Mode Structure Analysis of Tilted Bragg Grating Refractometers in Planar Waveguides Toward Absolute Index Measurement

Keith R. Daly,[1] Christopher Holmes,[2] James C. Gates,[2] Peter G. R. Smith,[2] and Giampaolo D'Alessandro[1]

[1]School of Mathematics, University of Southampton, SO17 1BJ Southampton, U.K.
[2]Optoelectronics Research Center, University of Southampton, SO17 1BJ Southampton, U.K.

DOI: 10.1109/JPHOT.2011.2168515
1943-0655/$26.00 ©2011 IEEE

Manuscript received July 27, 2011; revised September 1, 2011; accepted September 2, 2011. Date of publication September 19, 2011; date of current version September 30, 2011. Corresponding author: K. R. Daly (e-mail: krd103@soton.ac.uk).

Abstract: Tilted Bragg grating refractometers are ideal devices for sensing applications. They work by diffracting light from a confined core mode into a series of well-defined cladding modes that are sensitive to the refractive index of an adjacent fluid. Using the Cauchy integral method, we find the modes of a ridge waveguide refractometer. To gain good agreement with the experiment, the method requires us to take into account the dispersion and the 2-D geometry of the waveguide. The resulting modes are then used to predict the coupling dips in the reflection spectrum. Comparison with experimental measurements verifies the ability of this method to accurately determine the mode structure in the waveguide and, with minimal calibration, the refractive index of the adjacent fluid with error less than 2×10^{-4} riu.

Index Terms: Waveguides, plasmonics, gratings, sensors.

1. Introduction

Optical and plasmonic waveguides are used for a wide variety of refractive index sensing applications [1]. There are several different designs used for such devices. These sensors use Surface Plasmon Resonance (SPR) [2], [3], long range SPR [4], interferometers [5], [6], resonators [7], and optical fibers with tilted and nontilted Bragg gratings [8].

Tilted Bragg gratings are often used in fiber-based sensors to diffract a well-confined core mode into a discrete set of cladding [9] or plasmonic modes [10]. The structure of these modes, which can be determined from the transmission spectrum of the fiber, is dependent on the surrounding refractive index. Tilted gratings are advantageous over the conventional nontilted devices as their core modes are insensitive to external perturbations. In addition, they do not require the lapping and polishing of a cladding layer or the use of hazardous chemical etchants, such as hydrofluoric acid [8], to expose the grating in the fiber core.

In contrast to the developments in fiber tilted Bragg gratings [9]–[14], little has been reported on planar geometries. This may be due to the difficulties in achieving a discrete set of resolvable cladding modes. Recently, our group has demonstrated the first device which achieves this through physically micromachining two trenches either side of an ultraviolet (UV) written tilted Bragg grating [15]. The major advantage and novelty of these devices is that the fluid is well

separated from the waveguide core and is contained in micromachined channels. The fabrication process used in these devices is very fast (10^{-3} ms^{-1} cutting speeds) and does not use hazardous chemical etchants. The size of these channels also means that they can be easily integrated in microfluidic devices.

In this paper, we provide the first steps toward a theoretical study of the mode structure of such devices. This study is verified through experimental comparison. The modes of the waveguide are found using the Cauchy integral method, which is a numerical method for finding the zeros of a complex valued function [16]. The use of this method to find the modes of an optical waveguide was initially developed by Anemogiannis and Glytsis [17]. This method is capable of accurately finding all the modes of a waveguide and, unlike similar methods [18], [19], requires no *a priori* knowledge of the number of modes. The dispersion relation of a waveguide, the solutions of which determine the mode indices, forms a multivalued Riemann surface; for details, see [20]. However, rather than searching through the different layers of the surface, it is easier and more efficient to use a conformal mapping technique to unfold this surface [21]. It is this approach that we follow here.

The Cauchy integral method has been widely used for different waveguide structures, including SPR sensors [2], [3], waveguides with superconducting layers [22], metal–insulator–metal waveguides [23], waveguides with surface corrugations [24], and liquid crystal waveguides [25]. Here, we apply it to provide a thorough understanding of the mode structure in dielectric waveguides, which will lead to waveguide optimization.

The approach described in this paper allows us to determine the refractive index of the measured fluid to a high level of accuracy over a large range using only a single calibration run making it ideal for monolayer measurements. The fitting procedure is a two-step process. First, the spectrum of the waveguide in air is fitted using a least squares method. This single calibration fit constrains all the physical parameters of the waveguide. Secondly, the spectrum of the waveguide is measured a second time with an oil of known refractive index adjacent to the waveguide. This set of data is compared with numerical results using the refractive index of the oil as an unconstrained fitting parameter. The resulting fit allows us to determine the refractive index of the oil with error less than 2×10^{-4} refractive index units (riu) after only a single calibration, which corresponds to 0.02% of the known value.

This paper is arranged as follows: In Section 2, we provide an overview of the theory and numerical implementation of the Cauchy integral method for a general analytic function. The application of this method for ridge waveguides is described in Section 3. In Section 4, we provide an experimental verification of the method using the ridge waveguide structure described in [15]. Finally, in Section 5, we discuss the importance of the results obtained and how these results can be extended to understand and optimize complex metal clad dielectric waveguides.

2. Contour Integration

Finding the modes of a waveguide can be reduced to finding the zeros of a complex valued analytic function. One of the more powerful methods of doing this is the Cauchy integral method [16]. This method, as applied to waveguides, is described in detail in [17]. Here, we provide a brief summary of it. Using the residue theorem, it is possible to prove that

$$S_k \equiv \frac{1}{2i\pi} \oint_C z^k \frac{f'(z)}{f(z)} dz = \sum_n \zeta_n^k \tag{1}$$

where $k = 0, 1, 2, \ldots$ and ζ_n is the n-th zero of the analytic function $f(z)$. The number of zeros of $f(z)$ within a given contour is given by S_0. Further application of (1) allows the locations of the zeros to be found. This is achieved by defining the polynomial

$$P(z) = \sum_{m=0}^{S_0} C_m z^m \tag{2}$$

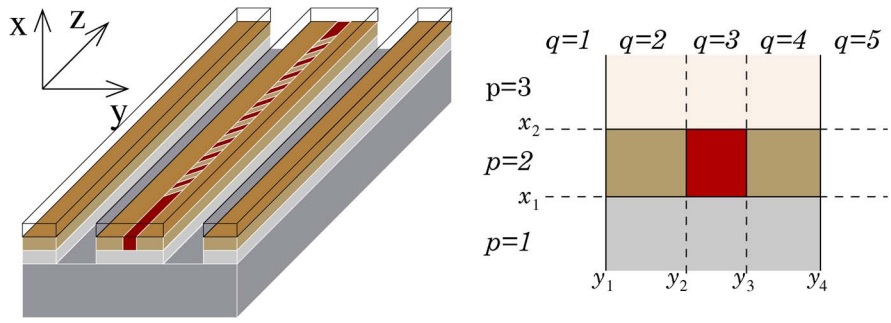

Fig. 1. Structure of ridge waveguide. Left-hand image shows schematic of waveguide structure. The right-hand image shows a cross-sectional area in the (x, y)-plane of the waveguide core and cladding layers.

such that the zeros of $P(z)$ coincide with the zeros of $f(z)$. The coefficients C_m are found recursively using the formula

$$C_m = \frac{1}{m - S_0} \sum_{j=1}^{S_0 - m} S_j C_{m+j} \tag{3}$$

with $C_{S_0} = 1$. The roots of the polynomial $P(z)$ can be found using standard numerical methods and, as a final step, are used as the starting point for a nonlinear root finding algorithm, e.g., Newton's.

There are several potential pitfalls in the implementation of this algorithm. First, numerical root-finding methods for polynomials are only accurate for low-order polynomials [26]. Therefore, for the method to be accurate, we require that the number of zeros of the function is small. In general, this requirement leads to subdivision of the initial contour. Second, should the integration contour pass directly through a zero, then S_k is singular. If this occurs, then the integration contour must be shifted away from this area.

To overcome these potential problems, a careful search of the initial contour is required. We start with a rectangular contour defined by the bounds on the refractive indices. Using (1), the number of zeros is computed. The numerical quadrature we are using is a Gauss–Kronrod Quadrature [27] with nodes and weights generated using the method of Laurie [28]. This method provides an approximation of the integral and an approximation of the numerical error. If either the error or the number of zeros found are too large, then the contour is divided. A typical maximum acceptable number of zeros per contour is 4. This procedure is repeated until convergence is reached. If the value of the integral in (1) is too large, then it is assumed that the integration contour is too close to a root. If this is the case, then the contour is shifted, and the integration is repeated.

Once the modes are isolated, the polynomial fitting and nonlinear root finding are standard and allows us to find the zeros of the function to high accuracy. We now consider how this method can be applied to ridge waveguides.

3. Modes of a Ridge Waveguide

3.1. Effective Index Method

We consider the propagation of light in the waveguide geometry shown in Fig. 1. We focus on the case where the electric field is predominantly in the y, z-plane. The aim of the effective index method is to reduce the ridge waveguide structure to two planar waveguide structures, the modes of which are found sequentially. Therefore, we shall adopt the planar waveguide notation of Transverse Magnetic (TM) and Transverse Electric (TE) polarization to denote modes with magnetic and

electric fields polarized in the x direction, respectively. As an example, we only derive the equations which describe the TM modes of a planar waveguide and highlight the required changes for TE modes. The TM modes can be described entirely in terms of their magnetic field, which we write as a series of modes

$$\mathcal{H}(\boldsymbol{x}) = \sum_j \hat{\boldsymbol{h}}_j H_j(x, y) e^{j(n_j k_0 z - \omega t)} \tag{4}$$

where $k_0 = 2\pi/\lambda$ is the free space wave number; λ is the free space wavelength; ω the optical angular frequency; and n_j, $\hat{\boldsymbol{h}}_j$, and $H_j(x, y)$ are the effective refractive index, polarization, and spatial profile of the j-th mode, respectively. We have also scaled space $\boldsymbol{x} = k_0 \tilde{\boldsymbol{x}}$, where $\tilde{\boldsymbol{x}}$ is the non-scaled spatial coordinate. The dielectric function for the structure is piecewise constant and is defined as $\epsilon(x, y) = \varepsilon_{p,q}$, where the regions p, q are defined in Fig. 1. Substituting (4) into Maxwell's equations we obtain the scalar Helmholtz equation for the magnetic field

$$\nabla^2 H_j + \left[n_j^2 - \epsilon(x, y)\right] H_j = 0. \tag{5}$$

Due to the complex geometry of the waveguide, there is no known analytic form for the solutions to (5). Therefore, in order to find the modes, we use the effective index method [29]. This is a two-stage method which allows us to approximate the 2-D waveguide structure, shown in Fig. 1, as a series of slab waveguides.

The first step is to consider each region q separately. For the ridge waveguides shown in Fig. 1, the region $p = 2$ is of higher index than the regions $p = 1, 3$. This creates a series of slab waveguides which must be solved for the TE solutions. The method by which these modes are found will be described in Section 3.2.

The ridge waveguides are designed such that the core in the x direction (region $p = 2$) is thin: typically $\pi(\tilde{x}_2 - \tilde{x}_1) < \lambda\sqrt{\varepsilon_{2,q}}$ for all q. Therefore, each individually considered slab waveguide will be single mode. The second stage in the effective index approximation is to use the mode indices for each slab $q = 1, 2, \ldots, 5$ as the refractive indices in each layer of the y-direction guide. The modes of the whole structure are given by the TM modes of this composite waveguide. The method for doing this will be described in Section 3.2. This approximate analysis has allowed us to reduce the problem to that of finding all the modes of several slab waveguides. The error induced by these approximations is relatively small because the waveguide is single mode in the x-direction, and therefore, the majority of the mode power is confined within the region $p = 2$.

3.2. Transfer Matrix

The modes of a slab waveguide can be found by solving Maxwell's equations in each region and matching the boundary conditions. Here, we consider only the TM polarized case in detail. The alterations required for the TE polarized case are also given. The starting point for this method is the Helmholtz equation for the magnetic field in each region

$$\frac{\partial^2 H_{j,q}}{\partial y^2} - \left[n_j^2 - \varepsilon_q\right] H_{j,q} = 0 \tag{6}$$

where the subscript j, q refers to the jth mode in region q, and we have dropped the subscript p from the dielectric function. For a given mode j, (6) has solutions

$$H_q = A_q \cos(i\gamma_q x) + B_q \sin(i\gamma_q x) \tag{7}$$

where $\gamma_q = \sqrt{n^2 - \varepsilon_q}$ are the transverse components of the wave vector, and for compactness of notation, we have dropped the subscript j. The boundary conditions for a TM wave require that H and $(1/\epsilon)\partial H/\partial x$ are continuous across each boundary and for a TE wave the electric field and its

normal derivative are continuous across each boundary. The field coefficients $\mathcal{V}_q = [A_q, B_q]^T$ are therefore linearly related to those in the following layer $\mathcal{V}_{q+1} = M_q \mathcal{V}_q$, where

$$M_q = \begin{pmatrix} \cos(i\gamma_q L_q) & -\frac{1}{\phi_q}\sin(i\gamma_q L_q) \\ \phi_q \sin(i\gamma_q L_q) & \cos(i\gamma_q L_q) \end{pmatrix}. \tag{8}$$

Here, $\phi_q = \gamma_q/\varepsilon_q$ and $\phi_q = \gamma_q$ for TM and TE polarizations, respectively, and L_q is the thickness of layer q. We consider only the finite set of bound modes and the countably infinite set of leaky modes [30]. Therefore, the solution in the two outer layers $q = 0$ and $q = N$ is

$$H_{0/N} = A_{0/N} e^{\gamma_{0/N} x} \tag{9}$$

where the sign associated with the real part of $\gamma_{0/N}$ determines whether the modes are bound or leaky in each of the semi-infinite external layers. Using (8) and (9), we find that bound or leaky modes can only propagate along the waveguide if the dispersion relation

$$F\left(n_j^2\right) \equiv \phi_0 T_{11} + \phi_0 \phi_N T_{12} + T_{21} + \phi_N T_{22} = 0 \tag{10}$$

is satisfied. Here, T_{ij} are the components of the transfer matrix for the internal layers, which is defined as

$$T = \prod_{q=1}^{N-1} M_q. \tag{11}$$

To proceed, we use the method of Smith *et al.* [21]. Equation (10) is an implicit function for the effective indices n_j. It turns out, due to the presence of the square roots which define the various γ_q, that this function is multivalued with branch cuts at the discontinuities $n^2 = (\varepsilon_0, \varepsilon_N)$. For a given n_j, there are four possible values for the function [20]. To overcome this, we make use of the mapping

$$u = \sqrt{n^2 - \varepsilon_0} + \sqrt{n^2 - \varepsilon_N} \tag{12}$$

to "unfold" the dispersion relation and map the singularities to the origin. The transverse components of the wave vector in terms of u are

$$\gamma_0 = \frac{u^2 + (\varepsilon_N - \varepsilon_0)}{2u} \tag{13a}$$

$$\gamma_N = \frac{u^2 - (\varepsilon_N - \varepsilon_0)}{2u} \tag{13b}$$

$$\gamma_q = \sqrt{\varepsilon_N + \gamma_N^2 - \varepsilon_q}, \quad (q \neq 0, N). \tag{13c}$$

Substituting these expressions into (10), we obtain that the modes of the waveguide correspond to the solutions of $\Psi(u) \equiv F(n(u)^2) = 0$. For the case of interest, here, $\varepsilon_0 = \varepsilon_N$. Therefore, (12), (13a), and (13b) reduce to $u = 2\sqrt{n^2 - \varepsilon_0}$, $\gamma_0 = \gamma_N = u/2$, removing the singularity at the origin. The Cauchy integral method can now be applied in terms of the independent variable u. The derivative of the dispersion relation for use in (1) is given in Appendix A. Typically, searches for the modes of a waveguide in the complex plane require multiple scans of different regions in order to find the guided, semileaky, and leaky modes. However, for a glass waveguide the leaky modes do not play a large part in determining the form of the reflection spectrum. Therefore, we need only search the region of the complex plane in which the guided modes are found [21], [31]. This is along the set interval of the real axis

$$\sqrt{|\varepsilon_N - \varepsilon_0|} \leq \Re(u) \leq \sqrt{\varepsilon_{max} - \varepsilon_0} + \sqrt{\varepsilon_{max} - \varepsilon_N}. \tag{14}$$

In practice, we search a thin strip around the real axis. As there is very little absorption in a glass only waveguide, this region can be correspondingly thin. Typically, we have used $-0.01 \leq \Im(u) \leq 0.01$,

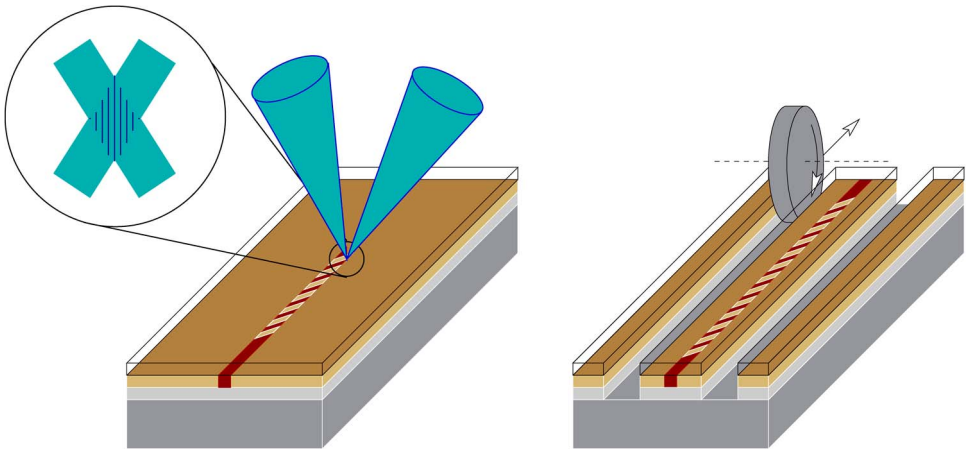

Fig. 2. Fabrication process. Left-hand image shows direct UV writing of waveguide and Bragg grating using two beam interferometer technique. Right-hand image shows cutting of trenches.

where this range has been chosen arbitrarily to have a nonzero thickness whilst only integrating a small area.

4. Experiment

4.1. Fabrication

The waveguide, as described in [15], is fabricated by first growing a 16.5 μm thermal oxide underclad on a 1 mm thick silicon wafer. Two silica layers, which form the core and overclad, are then deposited and consolidated using flame hydrolysis deposition (FHD). The core layer is 6.2 μm thick, and the overclad is 15.1 μm thick. The core layer is doped with germanium and boron to provide UV photosensitivity. This is further enhanced through hydrogen loading for 1 week at 12 MPa prior to UV writing.

The single mode waveguide and Bragg grating is fabricated using a dual beam interferometer technique [32], illustrated in Fig. 2. The technique involves interfering two coherent UV laser beams to create a single spot of width 6 μm. The interference pattern has period 540 nm, and the grating vector is tilted in the (y, z)-plane at an angle θ with respect to the z axis. To fabricate the channel waveguide and Bragg grating, the sample is translated, using a set of high precision translation stages, beneath the focused beams. This technique defines only a few periods per exposure before translation by a single period. Therefore, the induced stitching error is expected to be roughly periodic, resulting in a slight broadening in the spectral response of the device.

Once the grating has been written, the ridge structure of the waveguide is created using a dicing saw (Loadpoint, Microace). The cuts were made using a 70 μm wide diamond impregnated nickel bonded blade. This technique is capable of cutting ridges as thin as 10 μm [9], [33]. The final fabricated device studied here is 40 μm wide and 10 mm long, with an 8-mm-long grating which is tilted by 10°.

Light is coupled into and out of the single mode core using a polarization maintaining (PM) fiber pigtail. This is secured using UV curing epoxy. After curing, the pigtail is mechanically robust and has a low coupling loss that is less than 0.3 dB.

4.2. Experimental Comparison

Experimental verification of the modes supported by the device is obtained from the transmission and reflection spectra measured using an optical spectrum analyzer with 10 pm resolution. Light is injected into the core mode of the waveguide at a range of different frequencies. As the light propagates through the waveguide, it is diffracted by the grating into the backward propagating

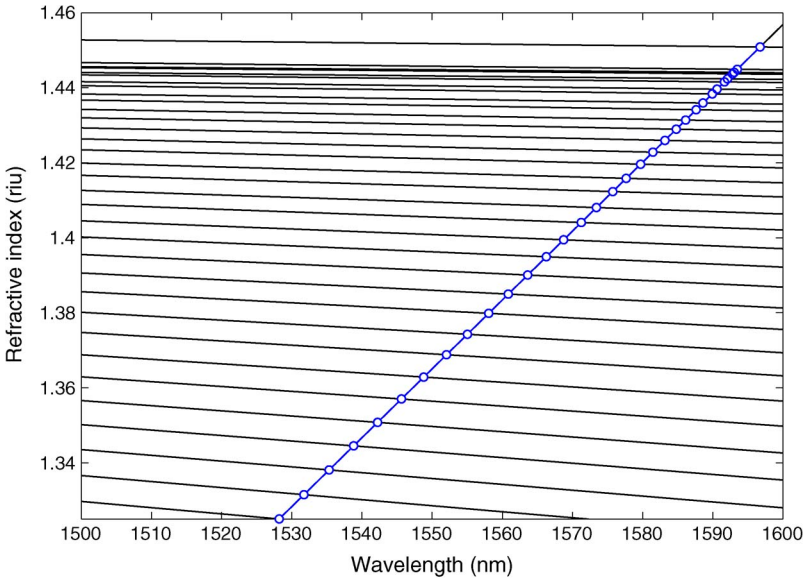

Fig. 3. Mode matching. The dispersion of the waveguide modes as calculated by the Cauchy integral method is given by the horizontal lines. The component of the diffracted wave vector in the direction of the mode propagation is shown by the diagonal line. Mode coupling occurs at the points where these lines cross (circles), resulting in a dip in the spectrum.

modes. Due to the experimental setup the measured spectrum is a superposition of the reflection and transmission spectra. Light diffracted into the backward propagating core mode is measured through the single fiber pigtail and is seen as a peak in the measured spectrum. The transmitted light is also measured due to the ≈4% Fresnel reflection from the glass air interface at the far end of the device. Therefore, the light diffracted from the core into the cladding modes is seen as a dip in the measured spectrum. Data is collected using an optical spectrum analyzer for a variety of different Cargille refractive index oils (series AAA and AA). Due to mode orthogonality, the grating must be tilted to allow efficient coupling between different modes. In order for the modes to be matched with zero phase detuning, we require

$$n_j(\lambda) = \frac{\lambda \cos\theta}{\Lambda} - n_0(\lambda) \tag{15}$$

where Λ is the grating period, and θ is the grating tilt angle in the y, z-plane with respect to the z-axis. The mode dispersion $n_j(\lambda)$ is calculated using the Cauchy integral method for a variety of wavelengths. The reflection dips will occur whenever the numerically calculated mode dispersion relations intersect (15); see Fig. 3.

The location of the spectral features are determined by fitting a Gaussian curve to each dip. The minimum of this curve is taken as the wavelength at which diffraction occurs. In order to accurately fit the experimental data, the waveguide dispersion relation must be taken into account. This is given by a Sellmeier equation with small corrections for the index of the core and cladding layers.

The physical parameters needed for the model are known to within a small uncertainty, i.e., ± 1 μm for the waveguide dimensions and $\pm 5 \times 10^{-3}$ for the refractive indices. To determine their value more precisely, we fit them in the absence of an index oil. The parameters used to obtain the initial fits are the guide width $W_g = \tilde{y}_4 - \tilde{y}_1 = 42.25$ μm, the core width $W_c = \tilde{x}_2 - \tilde{x}_1 = \tilde{y}_3 - \tilde{y}_2 = 5.50$ μm, the projected grating pitch $\Lambda_g = 549.1$ nm, the offset of the core from the center of the guide $\delta W = 0.09$ μm, and the refractive indices, which are given by a Sellmeier equation [34]. The variation in index in the different layers is given by a constant corrections to the Sellmeier equations: $\delta n_{uc} = -3.8 \times 10^{-3}$, $\delta n_{oc} = -3.1 \times 10^{-3}$, $\delta n_{co} = 9.5 \times 10^{-3}$, and $\delta n_{cl} = -1.4 \times 10^{-3}$ in the underclad, overclad, core, and cladding regions, respectively. This gives refractive indices $n_{uc} = 1.4440$,

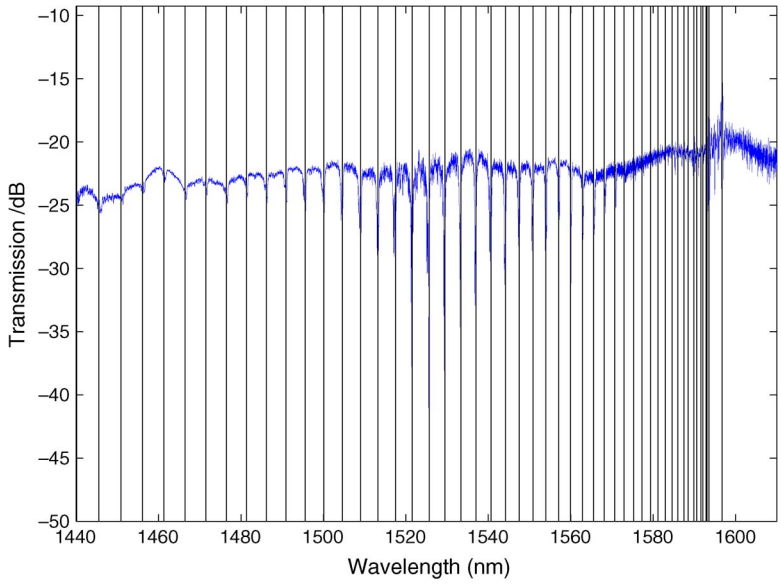

Fig. 4. Experimental spectrum (blue) and theoretical waveguide modes (vertical black lines) with air in the channels adjacent to the waveguide. Theoretical model is fitted using parameters described in the text.

$n_{oc} = 1.4447$, $n_{cl} = 1.4464$, and $n_{co} = 1.4573$ in the underclad, overclad, cladding, and core at $\lambda = 1550$ nm, respectively.

Once a fit has been obtained (see Fig. 4), the same parameters are used for the same waveguide but with an oil with known dispersion relation in the trenches. The verification process is repeated for a range of refractive index oils from $n_{\text{oil}} = 1.2962$ to $n_{\text{oil}} = 1.4298$ at $\lambda = 1550$ nm with high-quality fits being obtained in all cases. An example fit for the case of $n_{\text{oil}} = 1.3250$ at $\lambda = 1550$ nm is shown in Fig. 5.

The fit is seen to be of very high quality with the reflection dips corresponding to the theoretical predictions with very small maximum error, typically 0.1 nm per mode. The spacing between the dips in the reflection spectrum is approximately 3.75 nm, giving an error of approximately 3% in calculating the location of each feature. On close inspection, we observe that each of the resonances displays multiple features. We believe that these features result from a chirping effect due to ridge width variation and not polarization effects which have been observed in other systems [35]. This is supported experimentally, as launching an orthogonal polarization (TE) into the device results in comparable spectral resonance features that are spectrally resolved from the features of the TM polarization.

The lowest wavelength dips in the reflection spectrum occur for modes which have effective index lower than the index oil. These correspond to leaky modes with high propagation loss and, therefore, have the majority of their power outside of the waveguide. For this reason, the coupling coefficient between the core mode and the leaky mode becomes very small, and only the leaky modes which are close to the guided mode cutoff can be seen. The quality of this fit in both the fitting case and the test case verify the model's ability to predict these modes and, hence, the accuracy of the modeling assumptions used.

In order to evaluate the accuracy of the model, we consider the case where the refractive index of the oil is not known *a priori*. The refractive index of the Cargille index oils is given in the form of a three term Cauchy equation. However, over the range of wavelengths measured experimentally, the refractive index has very little change: $\sim O(10^{-6})$ riu nm^{-1}. Therefore, we assume a constant refractive index n_{oil} over the range of interest.

By using this value as a fitting parameter, it is possible to accurately determine the index of the fluid. For the example case $n = 1.3250$ at $\lambda = 1550$ nm, the refractive index of minimum error is

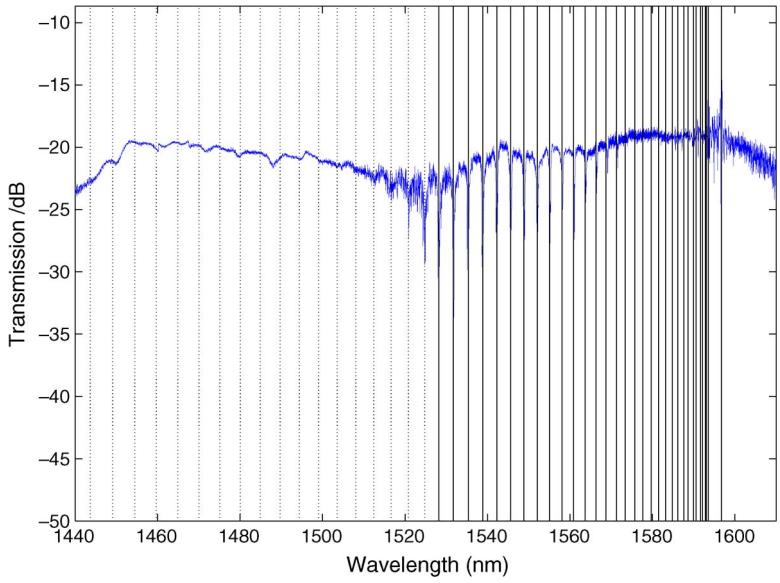

Fig. 5. Experimental spectrum (blue) and theoretical waveguide guided (vertical black lines) and leaky (dotted black lines) modes with oil in the channels adjacent to the waveguide. The waveguide parameters were fitted using the experimental data in air. No fitting parameters are used in the comparison with the oil data.

$n_{oil} = 1.3249$, which corresponds to a maximum refractive index error of 2×10^{-4} in the wavelength range tested. The fit has average error of 0.15 nm per mode and is seen to increase to approximately 0.17 nm per mode for $n_{oil} = 1.33$ or $n_{oil} = 1.32$, the two Cargille refractive index oils having values adjacent to the one used. It may be possible to determine the dispersion of the oil to a higher degree of accuracy if a device with a larger spectral bandwidth was used. However, from the measurements conducted here, only the constant part of the refractive index can be accurately found.

5. Discussion and Conclusion

The understanding of the mode structure of tilted Bragg grating waveguides for biosensors is of fundamental importance if these devices are to be optimized and used for sensing applications. The theoretical analysis presented here forms the groundwork for future experimental measurements and theoretical studies of these waveguides.

The use of the effective index approximation to reduce the ridge waveguide structure to a series of slab waveguides does not detract from the quality of the fit. The combination of the effective index method, the Cauchy integral method and the materials dispersion relations provides a complete description of the underlying mode structure.

Through careful analysis of the model, it can be seen that the dispersion of the waveguide and the application of the effective index method are key to obtaining precise fits. The accuracy of the model is shown by fitting the refractive index to the experimentally determined spectrum. This allows us to determine the refractive index at a given optical frequency precisely, with error less than 10^{-4}, over a large range with only a single calibration. These properties make this method ideal for low-index sensing applications, including refractive index measurement of monolayers in air.

There are several potential methods which could be used to increase the accuracy of the sensor. Surface roughness and core alignment play an important role in the spectral response of the refractometer. Decreased tolerance in the core alignment and flame brushing of the guide is expected to increase the uniformity in the guide and, hence, increase the signal-to-noise ratio. Further increases in sensitivity could also be achieved using a higher resolution spectrometer providing resolutions as low as 0.1 pm in contrast with 10 pm used in this paper.

There are two immediate extensions of this method to optimize waveguides for sensing. The first is the inclusion of a thin gold layer to the outside of the waveguide. This will allow the structure to support the highly sensitive plasmonic modes which are required for the most precise of sensing. The second is the study of the mode–mode interactions to optimize the coupling between sensing modes and core modes. Both of these extensions are work in progress.

The accuracy of this fitting will be of fundamental importance in the design and optimization of planar waveguide structures for sensing applications. The theory outlined here is of very general application and will provide the means to increase the sensitivity of such devices and their integration to become a reality.

Appendix

In this Appendix we provide expressions for the derivative of (10). Whilst the original method used a contour integral method to obtain this [17], it is computationally more efficient and accurate to differentiate (10) through repeated application of the chain rule:

$$\Psi'(u) = \phi_0 T'_{11} + \phi_0\phi_N T'_{12} + T'_{21} + \phi_N T'_{22} + (T_{11} + \phi_N T_{12})\phi'_0 + (T_{22} + \phi_0 T_{12})\phi'_N \tag{16}$$

$$T' = \sum_{q=1}^{N-1}\left\{\left[\prod_{k=1}^{q-1} M_k\right] M'_q \left[\prod_{k=q+1}^{N-1} M_k\right]\right\} \tag{17}$$

$$M'_q = \begin{pmatrix} -iL_q\gamma'_q \sin(i\gamma_q L_q) & -\frac{iL_q}{\phi_q}\gamma'_q \cos(i\gamma_q L_q) + \frac{\phi'_q}{\phi_q^2}\sin(i\gamma_q L_q) \\ \phi_q iL_q\gamma'_q \cos(i\gamma_q L_q) + \phi'_q \sin(i\gamma_q L_q) & -iL_q\gamma'_q \sin(i\gamma_q L_q) \end{pmatrix} \tag{18}$$

where $\phi'_q = \lambda'_q$ in the TE case, and $\phi'_q = \lambda'_q/\varepsilon_q$ in the TM case. Finally

$$\gamma'_q = \left(\varepsilon_N - \varepsilon_q + \gamma_N^2\right)^{-\frac{1}{2}}\gamma_N\gamma'_N \tag{19}$$

$$\gamma'_0 = 1 - \frac{u^2 + (\varepsilon_N - \varepsilon_0)}{2u^2} \tag{20}$$

$$\gamma'_N = 1 - \frac{u^2 - (\varepsilon_N - \varepsilon_0)}{2u^2}. \tag{21}$$

References

[1] X. Fan, M. White, S. I. Shopova, H. Zhu, J. D. Suter, and Y. Sun, "Sensitive optical biosensors for unlabeled targets: A review," *Anal. Chim. Acta*, vol. 620, no. 1/2, pp. 8–26, Jul. 2008.

[2] R. D. Harris and J. S. Wilkinson, "Waveguide surface plasmon resonance sensors," *Sens. Actuators B, Chem.*, vol. 29, no. 1–3, pp. 261–267, Oct. 1995, *Proc. 2nd Eur. Conf. Optical Chemical Sensors Biosensors.*

[3] R. D. Harris, B. J. Luff, J. S. Wilkinson, J. Piehler, A. Brecht, G. Gauglitz, and R. A. Abuknesha, "Integrated optical surface plasmon resonance immunoprobe for simazine detection," *Biosens. Bioelectron.*, vol. 14, no. 4, pp. 377–386, Apr. 1999.

[4] R. Slavik and J. Homola, "Ultrahigh resolution long range surface plasmon-based sensor," *Sens. Actuators B, Chem.*, vol. 123, no. 1, pp. 10–12, Apr. 2007.

[5] R. G. Heideman and P. V. Lambeck, "Remote opto-chemical sensing with extreme sensitivity: Design, fabrication and performance of a pigtailed integrated optical phase-modulated Mach-Zehnder interferometer system," *Sens. Actuators B, Chem.*, vol. 61, no. 1–3, pp. 100–127, Dec. 1999.

[6] A. Brandenburg, "Differential refractometry by an integrated-optical Young interferometer," *Sens. Actuators B, Chem.*, vol. 39, no. 1–3, pp. 266–271, Mar./Apr. 1997, *3rd Eur. Conf. Optical Chemical Sensors Biosensors.*

[7] C. A. Barrios, K. B. Gylfason, B. Sánchez, A. Griol, H. Sohlström, M. Holgado, and R. Casquel, "Slot-waveguide biochemical sensor," *Opt. Lett.*, vol. 32, no. 21, pp. 3080–3082, Nov. 2007.

[8] G. Meltz, S. J. Hewlett, and J. D. Love, "Fiber grating evanescent-wave sensors," *Proc. SPIE*, vol. 2836, pp. 342–350, Dec. 1996.

[9] T. Guo, H. Tam, P. A. Krug, and J. Albert, "Reflective tilted fiber Bragg grating refractometer based on strong cladding to core recoupling," *Opt. Express*, vol. 17, no. 7, pp. 5736–5742, Mar. 2009.

[10] Y. Y. Shevchenko and J. Albert, "Plasmon resonances in gold-coated tilted fiber Bragg gratings," *Opt. Lett.*, vol. 32, no. 3, pp. 211–213, Feb. 2007.

[11] T. Erdogan and J. E. Sipe, "Tilted fiber phase gratings," *J. Opt. Soc. Amer. A, Opt. Image Sci.*, vol. 13, no. 2, pp. 296–313, Feb. 1996.

[12] Y. C. Lu, W. P. Huang, and S. S. Jian, "Full vector complex coupled mode theory for tilted fiber gratings," *Opt. Express*, vol. 18, no. 2, pp. 713–725, Jan. 2010.
[13] T. Guo, C. Chen, and J. Albert, "Non-uniform-tilt-modulated fiber Bragg grating for temperature-immune micro-displacement measurement," *Meas. Sci. Technol.*, vol. 20, no. 3, p. 034007, Mar. 2009.
[14] L. Shao, Y. Shevchenko, and J. Albert, "Intrinsic temperature sensitivity of tilted fiber Bragg grating based surface plasmon resonance sensors," *Opt. Express*, vol. 18, no. 11, pp. 11 464–11 471, May 2010.
[15] C. Holmes, L. G. Carpenter, H. L. Rogers, I. J. G. Sparrow, J. C. Gates, and P. G. R. Smith, "Planar waveguide tilted Bragg grating refractometer fabricated through physical micromachining and direct UV writing," *Opt. Express*, vol. 19, no. 13, pp. 12 462–12 468, Jun. 2011.
[16] L. M. Delves and J. N. Lyness, "A numerical method for locating the zeros of an analytic function," *Math. Comput.*, vol. 21, no. 100, pp. 543–560, Oct. 1967.
[17] E. Anemogiannis and E. N. Glytsis, "Multilayer waveguides: Efficient numerical analysis of general structures," *J. Lightw. Technol.*, vol. 10, no. 10, pp. 1344–1351, Oct. 1992.
[18] L. F. Abdella, L. M. Delves, and J. K. Ried, "A numerical method for locating the zeros and pole of a meromorphic functional," in *Numerical Methods for Non-Linear Algebraic Equations*. London, U.K.: Gordon and Breach, 1970, pp. 47–50.
[19] E. Anemogiannis, E. N. Glytsis, and T. K. Gaylord, "Efficient solution of eigenvalue equations of optical waveguiding structures," *J. Lightw. Technol.*, vol. 12, no. 12, pp. 2080–2084, Dec. 1994.
[20] R. E. Smith, S. N. Houde-Walter, and G. W. Forbes, "Mode determination for planar waveguides using the four-sheeted dispersion relation," *IEEE J. Quantum Electron.*, vol. 28, no. 6, pp. 1520–1526, Jun. 1992.
[21] R. E. Smith, G. W. Forbes, and S. N. Houde-Walter, "Unfolding the multivalued planar waveguide dispersion relation," *IEEE J. Quantum Electron.*, vol. 29, no. 4, pp. 1031–1034, Apr. 1993.
[22] B. G. Ghamsari and A. H. Majedi, "Rigorous analysis of superconducting multilayer optical waveguides," *IEEE Trans. Appl. Supercond.*, vol. 17, no. 2, pp. 590–593, Jun. 2007.
[23] Ş E. Kocabaş, G. Veronis, D. A. B. Miller, and S. Fan, "Modal analysis and coupling in metal-insulator-metal waveguides," *Phys. Rev. B, Condens. Matter*, vol. 79, no. 3, p. 035120, Jan. 2009.
[24] Q. Liu and K. S. Chiang, "Refractive-index sensor based on long-range surface plasmon mode excitation with long-period waveguide grating," *Opt. Express*, vol. 17, no. 10, pp. 7933–7942, May 2009.
[25] D. B. Walker, E. N. Glytsis, and T. K. Gaylord, "Ferroelectric liquid-crystal waveguide modulation based on a switchable uniaxial–uniaxial interface," *Appl. Opt.*, vol. 35, no. 16, pp. 3016–3030, Jun. 1996.
[26] J. H. Wilkinson, "The perfidious polynomial," in *Studies in Numerical Analysis*. Washington, DC: MAA, 1984, pp. 1–28.
[27] A. S. Kronrod, *Nodes and Weights of Quadrature Formulas: Sixteen-Place Tables*. New York: Consultants Bureau, 1965.
[28] D. P. Laurie, "Calculation of Gauss-Kronrod quadrature rules," *Math. Comput.*, vol. 66, no. 219, pp. 1133–1145, Jul. 1997.
[29] K. Okamoto, *Fundamentals of Optical Waveguides*. New York: Academic, 2000.
[30] T. Tamir, "Inhomogeneous wave types at planar structures: III. Leaky waves," *Optik*, vol. 38, no. 3, pp. 269–297, 1973.
[31] D. Stowell and J. Tausch, "Guided and leaky modes of planar waveguides: Computation via higher order finite elements and iterative methods," *PIERS Online*, vol. 6, no. 7, pp. 669–673, 2010.
[32] G. D. Emmerson, S. P. Watts, C. B. E. Gawith, V. Albanis, M. Ibsen, R. B. Williams, and P. G. R. Smith, "Fabrication of directly UV-written channel waveguides with simultaneously defined integral Bragg gratings," *Electron. Lett.*, vol. 38, no. 24, pp. 1531–1532, Nov. 2002.
[33] X. Chen, K. Zhou, L. Zhang, and I. Bennion, "Optical chemsensor based on etched tilted Bragg grating structures in multimode fiber," *IEEE Photon. Technol. Lett.*, vol. 17, no. 4, pp. 864–866, Apr. 2005.
[34] H. L. Rogers, C. Holmes, J. C. Gates, and P. G. R. Smith, "Direct refractive index measurement technique to observe waveguide dispersion characteristics of short waveguides utilising the higher order modes of integrated Bragg grating structures," presented at the Eur. Conf. Lasers Electro-Optics Quantum Electron. Conf., Munich, Germany, 2011, Paper CE1_1.
[35] Y. C. Lu, R. Geng, C. Wang, F. Zhang, C. Liu, T. Ning, and S. Jian, "Polarization effects in tilted fiber Bragg grating refractometers," *J. Lightw. Technol.*, vol. 28, no. 11, pp. 1677–1684, Jun. 2010.